The divergent fates of primitive hydrospheric water on Earth and Mars

Wade, Jon; Dyck, Brendan; Palin, Richard M.; Moore, James Daniel Paul; Smye, Andrew J.

2017

Wade, J., Dyck, B., Palin, R. M., Moore, J. D. P., & Smye, A. J. (2017). The divergent fates of primitive hydrospheric water on Earth and Mars. Nature, 552, 391-394.

https://hdl.handle.net/10356/86885

https://doi.org/10.1038/nature25031

The divergent fates of primitive hydrospheric water on Earth and Mars

Jon Wade[1]*, Brendan Dyck[2,6], Richard M. Palin[3], James D.P. Moore[4], Andrew J. Smye[5]

[1] Department of Earth Sciences, University of Oxford, South Parks Road, Oxford OX1 3AN, UK

[2] Department of Earth Sciences, University of Cambridge, Cambridge, CB2 3EQ, UK

[3] Department of Geology and Geological Engineering, Colorado School of Mines, Golden, CO 80401, USA

[4] Earth Observatory of Singapore, Nanyang Technological University, Singapore

[5] Department of Geosciences, Pennsylvania State, PA 16801, USA

[6] Department of Earth Sciences, Simon Fraser University, Burnaby, BC, V5A 1S6, Canada

* corresponding author: *jon.wade@earth.ox.ac.uk*

Despite active transport mechanisms into the Earth's mantle, water has been present on our planet's surface for most of geological time[1,2], yet water disappeared from the Martian surface soon after its formation. While the Martian water inventory was partially depleted by loss to space via photolysis following the collapse of the planet's magnetic field[3-5], widespread serpentinisation of Martian crust[6,7] attests to metamorphic hydration reactions having played a critical role in its sequestration. Here we quantify the relative volumes of water that could be removed from each planet's surface via the burial and metamorphism of hydrated mafic crusts, and calculate mineral transition-induced bulk-density changes at elevated pressure–temperature conditions in each. The metamorphic mineral assemblages in relatively FeO-rich Martian lavas can hold ~25% more structurally-bound H_2O than those in metamorphosed terrestrial basalts, and transport it to greater relative depths

within the Martian interior. Our calculations suggest that in excess of 9 vol. % of the Martian mantle may contain hydrous mineral species as a consequence of surface reactions, compared to ~4 vol. % of the Earth. Furthermore, neither primitive nor evolved hydrated Martian crust show significantly different bulk densities compared to their anhydrous equivalents, in contrast to mafic terrestrial crust that transforms to eclogite upon dehydration. This would have allowed efficient over-plating and burial of early Martian crust in a stagnant lid tectonic regime, thus providing a significant sink for hydrospheric water and a mechanism to oxidise the Martian mantle. Conversely, relatively buoyant mafic crust and hotter geothermal gradients on Earth reduced the potential for upper mantle hydration early in its geological history, leading to water being retained close to its surface, thus creating conditions conducive for the evolution of complex multicellular life.

Surface water has existed on Earth for the vast majority of geologic time[1], with its volume having remained approximately constant since the end of the Archean (2.5 Ga) and initiation of subduction-driven plate tectonics[2]. However, despite evidence for it having once possessed liquid water, the modern-day surface of Mars is essentially dry and lacks any widespread features of active plate tectonics[8]. The loss of surficial water from Mars since its formation has been attributed to both photolysis in the upper atmosphere and/or sequestration into the crust via metamorphic hydration reactions[9]. Although loss to space by atmospheric sputtering and hydrodynamic escape likely became increasingly viable after cessation of the Martian magnetic field at c. 4.1 Ga[3-5], uncertainties in its efficiency, the timing of field collapse, and the initial water inventory suggest that this process alone may not have depleted the entire volume of the hydrosphere over the lifetime of the planet[10-12]. Instead, petrological evidence for crustal hydration—a notably more efficient mechanism to sequester large amounts of H_2O from a planet's hydrosphere—is present as serpentinized surface basalts[6,7] and the widespread distribution of oxidised hydrated phyllosilicate minerals[7]. The disassociation of water during such

52 silicate-mineral hydration reactions and the subsequent loss of hydrogen to space, for example,
53 may account for the presence of oxidised magnetite[13] and maghemite in Martian meteorite
54 NWA7034 and the Gusev crater rocks it resembles[14], while the source region of Martian SNC
55 meteorites is much more reduced[14,15].
56
57 Aside from the proportion of iron, the terrestrial and Martian mantles have broadly similar
58 chondritic major element compositions[16,17]. The abundance of iron in planetary mantles—and
59 hence erupted surface material—is primarily controlled by the prevailing oxygen fugacity (fO_2)
60 of planetary accretion, which was higher during Martian core formation than terrestrial core
61 formation. As a result, terrestrial basalts are relatively FeO-poor (~7–10 wt. %)[18] compared to
62 more FeO-rich (~17 wt. %)[19] basalts derived from the Martian upper mantle. As bulk-rock
63 composition is the primary control on the mineral assemblages that stabilise during surface
64 hydration and metamorphism at elevated pressure (P) and temperature (T) conditions, these
65 compositional differences likely played a critical role in controlling each planet's bulk
66 geochemistry and surface water budget over geological time. Here, we have quantified the
67 balance between mantle hydration and density in both terrestrial and Martian interiors using
68 integrated thermal and petrological modelling. We show that metamorphosed primitive and
69 evolved Martian basalts can hold ~25% more structurally-bound water in hydrous minerals than
70 terrestrial equivalents can, with the majority stable to greater depths within Mars (>90 km) than
71 within Earth (~70 km). In addition, time-integrated mass-balance calculations show that the
72 absolute volume of the Martian mantle that has potentially been hydrated over geological time
73 (>9%) is at least twice as large as the terrestrial mantle (~4%).
74
75 Although achieved at different times in their cooling histories, in order to model their surface
76 evolutions we considered a mantle potential temperature (T_P) of 1650 °C for both the terrestrial
77 and Martian primitive basalts, and a lower bound of 1400 °C for evolved rocks. SNC meteorites

indicate that the rate of secular cooling on Mars was conservatively about three-times faster than that of Earth[20]. We combined this with a plate cooling model, taking into account secular cooling and radiogenic heat production in order to calculate likely aerotherms and geotherms through the lithospheres of each planet. The petrological changes that would occur in the end member cases of primitive and evolved, fully hydrated and fluid-undersaturated crust during each planet's geological evolution were then investigated using thermodynamic phase equilibrium modelling at conditions defined by these *P–T* gradients. For Mars, we utilised bulk compositions for primitive (Fastball) and evolved (Backstay) basalts, and for Earth we utilised a high-MgO Archean tholeiitic basalt and a modern-day MORB (see *Methods*). We considered metamorphism at pressures of 8–26 kbar (Earth) and 3–10 kbar (Mars), and temperatures of 500–1200 °C. Hydration at lower-grade conditions is controlled by phases belonging to the serpentine, phyllosilicate, and clay mineral groups, with higher water contents. Phase diagrams for each rock type considering fluid-saturated conditions are presented in *Extended data* Figures 1–4.

Calculated water contents and bulk-rock densities for each terrestrial and Martian protolith as a function of depth within the planetary interior are shown in Figure 1. Unlike terrestrial modern MORB, the higher water-carrying potential of high-MgO Archean terrestrial basalts is primarily a result of their more refractory nature, with the absence of quartz allowing water-bearing amphiboles to persist to higher temperatures[21], and thus greater depths in the mantle (Figure 1a). A similar trend characterises Martian materials, with metamorphosed primitive basalt (Fastball) being comprised mostly of hornblendic amphibole at subsolidus *P–T* conditions. Evolved Martian melts (Backstay-type compositions) contain a smaller proportion of water-bearing minerals at these temperatures, but retain their water to greater depths. In both cases, the net water-bearing potential of Martian materials exceed those of their terrestrial counterparts.

103 The decomposition of amphibole during prograde metamorphism marks the terminus of hydrous
104 mineral stability in both terrestrial and Martian materials. Indeed, evolved Martian basalts may
105 retain amphibole to temperatures in excess of 1200 °C, where they are calculated to become Ti-
106 rich, matching observed compositions from Martian meteorites[22]. Although hydration extends to
107 similar absolute depths on both bodies, the shallower Martian aerotherm implies that the volume
108 fraction of silicate Mars that may be hydrated following crustal subduction is about double that of
109 the Earth (Figure 2). Additionally, the faster cooling of Mars[20] progressively extends the depth of
110 hydration, exacerbated by the presence of more evolved basalts over-plating the Martian surface
111 and the negative Clapeyron slope for hornblende dehydration. The effect that hydration has on
112 bulk-rock density heightens this effect; metamorphosed terrestrial basalts are all significantly less
113 dense—and hence buoyant—when fluid-saturated, and undergo densification upon dehydration
114 (Figure 1b). The relatively Fe-rich Martian materials are, however, calculated to exhibit relatively
115 little volume expansion during hydration, with more evolved basalts showing minimal change in
116 bulk-rock density, and significant densification (>5%) of a water-bearing restite, post-melting.
117 Here, the main reaction products of high-pressure hornblende dehydration at the fayalite–
118 magnetite–quartz (FMQ) buffer are clinopyroxene, plagioclase, garnet, magnetite, and silicate
119 melt.
120
121 Hydrated Martian basalts generate relatively high degrees of melt (~30%) at moderate
122 temperatures (~800–900 °C), leaving a hydrous residual assemblage of neutral or negative
123 buoyancy. This suggests that, unlike on Earth, hydrated materials could have been transferred
124 into its mantle via sagduction or crustal delamination[23,24] (Figure 3). Mars may therefore have
125 undergone extensive hydration of its mantle simply by magmatic overplating, burial and
126 metamorphism of hydrated surface basalts. This mechanism may also have been responsible for
127 delivering oxidised material to the source region of the Martian surface basalts[14]. On Earth, the
128 increased buoyancy of hydrated Archaean greenstones and steeper geotherm limit the water-

carrying capacity of over-plated material. The secular evolution of plate tectonics and the transition from early-Earth high-MgO basalts to modern-day MORB basalts (with an inherently lower water-carrying capacity)[25] further limits the mechanisms of water transport into the terrestrial interior. Mars shows the opposite trend, as its secular cooling, high water-carrying capacity of surface basalts, and the neutral buoyancy of hydrated materials acted to preferentially sequester water back into its interior.

On Earth, surface water is transported into the upper mantle primarily by K-amphibole[26], which typically forms in hydrated MgO-rich metabasalt. In contrast, more ferruginous Martian basalts stabilize iron-rich hydrous phases at equivalent *P–T* conditions, such as hornblende and biotite (Extended Data - Figure 5). The decomposition of hornblendic amphibole during metamorphism is controlled by *P*, *T*, and fO_2, with lower temperatures and reducing conditions specifically favouring its stability[27]. Owing to its smaller size, Martian aerotherms have higher d*T*/d*P* gradients than geotherms on Earth, which suggests that hydrous phases, such as amphibole, comprise a greater proportion of its mantle. Rock-hydration reactions may therefore be important both as a surface water-loss mechanism and as a means to transport oxidised material to upper-mantle depths. However, as hydration reactions are typically associated with a decrease in bulk-rock density, re-entrainment of crustal material into the mantle—either via burial or subduction—may be limited until dehydration has occurred.

In the absence of subduction-driven plate tectonics early in each planet's geologic history[28], both Earth and Mars would have experienced significant basaltic surface over-plating. Elevated mantle potential temperatures would have led to higher degrees of partial melting and more voluminous, low-viscosity magmas. Erupted[29] or emplaced[30] in the presence of water, they may be assumed to efficiently hydrate[31]. Our results show that the ability of a planet to retain surface water is not simply a function of its bulk composition or size, but also its accretion history, not least the

oxygen fugacities prevailing during core formation. By setting the bulk silicate FeO content, mantle redox state places a first-order control on the amount of amphibole production and stability, and hence high-pressure water-carrying minerals. Earth-like planetary size allows a long-lived steep geotherm, which in turn promotes dewatering of hydrated phases close to the planetary surface, and thus the efficient return of buried water to the surface (Figure 1). In contrast, Mars exhibits evidence of long-lived water reservoirs both extant as sub-surface ice[32] and as hydrated crust[33]. These, together with the elevated FeO contents of the Martian mantle and smaller planetary size, results in significant water sequestration into the Martian mantle via increased amphibole content and the production of hydrous restite of neutral or negative buoyancy. Taken concurrently, the individual water-carrying capacities of erupted magmas and their respective fates upon burial are key to understanding the early hydrological cycles on each planet.

Acknowledgments: JW acknowledges receipt of an NERC Independent Research Fellowship NE/K009540/1. J.D.P.M was supported by the National Research Foundation (NRF) of Singapore under the NRF Fellowship scheme (National Research Fellow award NRF-NRFF2013-04) and by the Earth Observatory of Singapore, the NRF, and the Singapore Ministry of Education under the Research Centres of Excellence initiative.

Author Contribution: J.W. conceived the idea in discussion with A.J.S. and performed initial calculations. R.M.P. and B.D. performed the petrological modelling. Thermal modelling was performed by J.D.P.M. All authors contributed to writing the final manuscript.

The authors declare no competing financial interests.

CAPTIONS

Figure 1 | Calculated petrophysical properties for each modelled basaltic protolith. a, Plot of the structurally-bound water content (wt. %) in metamorphosed primitive and evolved basalt on Earth and Mars. **b**, Relative density deficit between a crustal column comprised of fully hydrated and nominally anhydrous metabasalt ($\delta\rho = (\rho_{anhydrous} - \rho_{hydrated})/\rho_{anhydrous}$).

Figure 2 | Degree of mantle hydration on Earth and Mars as a function of dewatering of metamorphosed basalts.

Figure 3 | Schematic cross sections through primitive (a) Martian and (b) terrestrial mafic crust. Lithological components of metamorphosed hydrated and nominally anhydrous mafic crusts on Earth and Mars based on calculated phase assemblages. Orange (Early Mars) and yellow (Early Earth) detail represent melt.

REFERENCES IN MAIN TEXT AND CAPTIONS

1 Peck, W. H., Valley, J. W., Wilde, S. A. & Graham, C. M. Oxygen isotope ratios and rare earth elements in 3.3 to 4.4 Ga zircons: Ion microprobe evidence for high δ18O continental crust and oceans in the early Archean. *Geochimica et Cosmochimica Acta* **65**, 4215-4229, doi:10.1016/S0016-7037(01)00711-6 (2001).

2 Korenaga, J. Thermal evolution with a hydrating mantle and the initiation of plate tectonics in the early Earth. *Journal of Geophysical Research: Solid Earth* **116**, n/a-n/a, doi:10.1029/2011JB008410 (2011).

3 Lillis, R. J. *et al.* An improved crustal magnetic field map of Mars from electron reflectometry: Highland volcano magmatic history and the end of the martian dynamo. *Icarus* **194**, 575-596, doi:http://dx.doi.org/10.1016/j.icarus.2007.09.032 (2008).

4 Acuña, M. H. *et al.* Global Distribution of Crustal Magnetization Discovered by the Mars Global Surveyor MAG/ER Experiment. *Science* **284**, 790 (1999).

5 Dubinin, E. *et al.* Effects of solar irradiance on the upper ionosphere and oxygen ion escape at Mars: MAVEN observations. *Journal of Geophysical Research: Space Physics* **122**, 7142-7152, doi:10.1002/2017JA024126 (2017).

6 Ehlmann, B. L., Mustard, J. F. & Murchie, S. L. Geologic setting of serpentine deposits on Mars. *Geophysical Research Letters* **37**, n/a-n/a, doi:10.1029/2010gl042596 (2010).

7 Carter, J., Poulet, F., Bibring, J. P., Mangold, N. & Murchie, S. Hydrous minerals on Mars as seen by the CRISM and OMEGA imaging spectrometers: Updated global view. *Journal of Geophysical Research: Planets* **118**, 831-858, doi:10.1029/2012je004145 (2013).

8 Yin, A. Structural analysis of the Valles Marineris fault zone: Possible evidence for large-scale strike-slip faulting on Mars. *Lithosphere* **4**, 286-330, doi:10.1130/L192.1 (2012).
9 Lammer, H. *et al.* Outgassing History and Escape of the Martian Atmosphere and Water Inventory. *Space Science Reviews* **174**, 113-154, doi:10.1007/s11214-012-9943-8 (2012).
10 Wordsworth, R. D. in *Annual Review of Earth and Planetary Sciences* Vol. 44 381-408 (2016).
11 Di Achille, G. & Hynek, B. M. Ancient ocean on Mars supported by global distribution of deltas and valleys. *Nature Geoscience* **3**, 459-463, doi:10.1038/ngeo891 (2010).
12 Carr, M. H. & Head, J. W. Martian surface/near-surface water inventory: Sources, sinks, and changes with time. *Geophysical Research Letters* **42**, 726-732, doi:10.1002/2014GL062464 (2015).
13 Chassefière, E., Langlais, B., Quesnel, Y. & Leblanc, F. The fate of early Mars' lost water: The role of serpentinization. *Journal of Geophysical Research E: Planets* **118**, 1123-1134, doi:10.1002/jgre.20089 (2013).
14 Tuff, J., Wade, J. & Wood, B. J. Volcanism on Mars controlled by early oxidation of the upper mantle. *Nature* **498**, 342-345, doi:10.1038/nature12225 (2013).
15 Wadhwa, M. Redox state of mars' upper mantle and crust from eu anomalies in shergottite pyroxenes. *Science* **291**, 1527-1530, doi:10.1126/science.1057594 (2001).
16 McDonough, W. F. & Sun, S.-s. The composition of the Earth. *Chemical Geology* **120**, 223-253 (1995).
17 Dreibus, G. & Wanke, H. Mars, A Volatile-Rich Planet. *Meteoritics* **20**, 367-381 (1985).
18 White, W. M. & Klein, E. M. in *Treatise on Geochemistry: Second Edition* Vol. 4 457-496 (2013).
19 Squyres, S. W. *et al.* Pyroclastic Activity at Home Plate in Gusev Crater, Mars. *Science* **316**, 738-742, doi:10.1126/science.1139045 (2007).
20 Lessel, J. & Putirka, K. New thermobarometers for martian igneous rocks, and some implications for secular cooling on Mars. *American Mineralogist* **100**, 2163-2171, doi:10.2138/am-2015-4732 (2015).
21 Hartel, T. H. D. & Pattison, D. R. M. Genesis of the Kapuskasing (Ontario) migmatitic mafic granulites by dehydration melting of amphibolite: The importance of quartz to reaction progress. *Journal of Metamorphic Geology* **14**, 591-611, doi:10.1046/j.1525-1314.1996.00404.x (1996).
22 Watson, L. L., Hutcheon, I. D., Epstein, S. & Stolper, E. M. Water on Mars - Clues from Deuterium/Hydrogen and Water Contents of Hydrous Phases in Snc Meteorites. *Science* **265**, 86-90 (1994).
23 Fischer, R. & Gerya, T. Early Earth plume-lid tectonics: A high-resolution 3D numerical modelling approach. *Journal of Geodynamics* **100**, 198-214, doi:10.1016/j.jog.2016.03.004 (2016).
24 Francois, C., Philippot, P., Rey, P. & Rubatto, D. Burial and exhumation during Archean sagduction in the East Pilbara Granite-Greenstone Terrane. *Earth and Planetary Science Letters* **396**, 235-251, doi:10.1016/j.epsl.2014.04.025 (2014).
25 Palin, R. M. & White, R. W. Emergence of blueschists on Earth linked to secular changes in oceanic crust composition. *Nature Geoscience* **9**, 60-64, doi:10.1038/ngeo2605 (2016).
26 Williams, Q. & Hemley, R. J. Hydrogen in the deep earth. *Annual Review Of Earth And Planetary Sciences* **29**, 365-418 (2001).
27 Gilbert, M. C. Synthesis and stability relations of the hornblende ferropargasite. *American Journal of Science* **264**, 698-742, doi:10.2475/ajs.264.9.698 (1966).
28 Carr, M. H. & Head Iii, J. W. Geologic history of Mars. *Earth and Planetary Science Letters* **294**, 185-203, doi:http://dx.doi.org/10.1016/j.epsl.2009.06.042 (2010).

29 Hauck, S. A. & Phillips, R. J. Thermal and crustal evolution of Mars. *Journal of Geophysical Research-Planets* **107**, doi:10.1029/2001je001801 (2002).
30 Viviano, C. E., Moersch, J. E. & McSween, H. Y. Implications for early hydrothermal environments on Mars through the spectral evidence for carbonation and chloritization reactions in the Nili Fossae region. *Journal of Geophysical Research: Planets* **118**, 1858-1872, doi:10.1002/jgre.20141 (2013).
31 Poli, S. & Schmidt, M. W. Petrology of subducted slabs. *Annual Review Of Earth And Planetary Sciences* **30**, 207-235 (2002).
32 Mouginot, J., Pommerol, A., Beck, P., Kofman, W. & Clifford, S. M. Dielectric map of the Martian northern hemisphere and the nature of plain filling materials. *Geophysical Research Letters* **39**, n/a-n/a, doi:10.1029/2011gl050286 (2012).
33 Usui, T., Alexander, C. M. O. D., Wang, J., Simon, J. I. & Jones, J. H. Meteoritic evidence for a previously unrecognized hydrogen reservoir on Mars. *Earth and Planetary Science Letters* **410**, 140-151, doi:10.1016/j.epsl.2014.11.022 (2015).

284 Fig1, 2 &3 (in order)
285

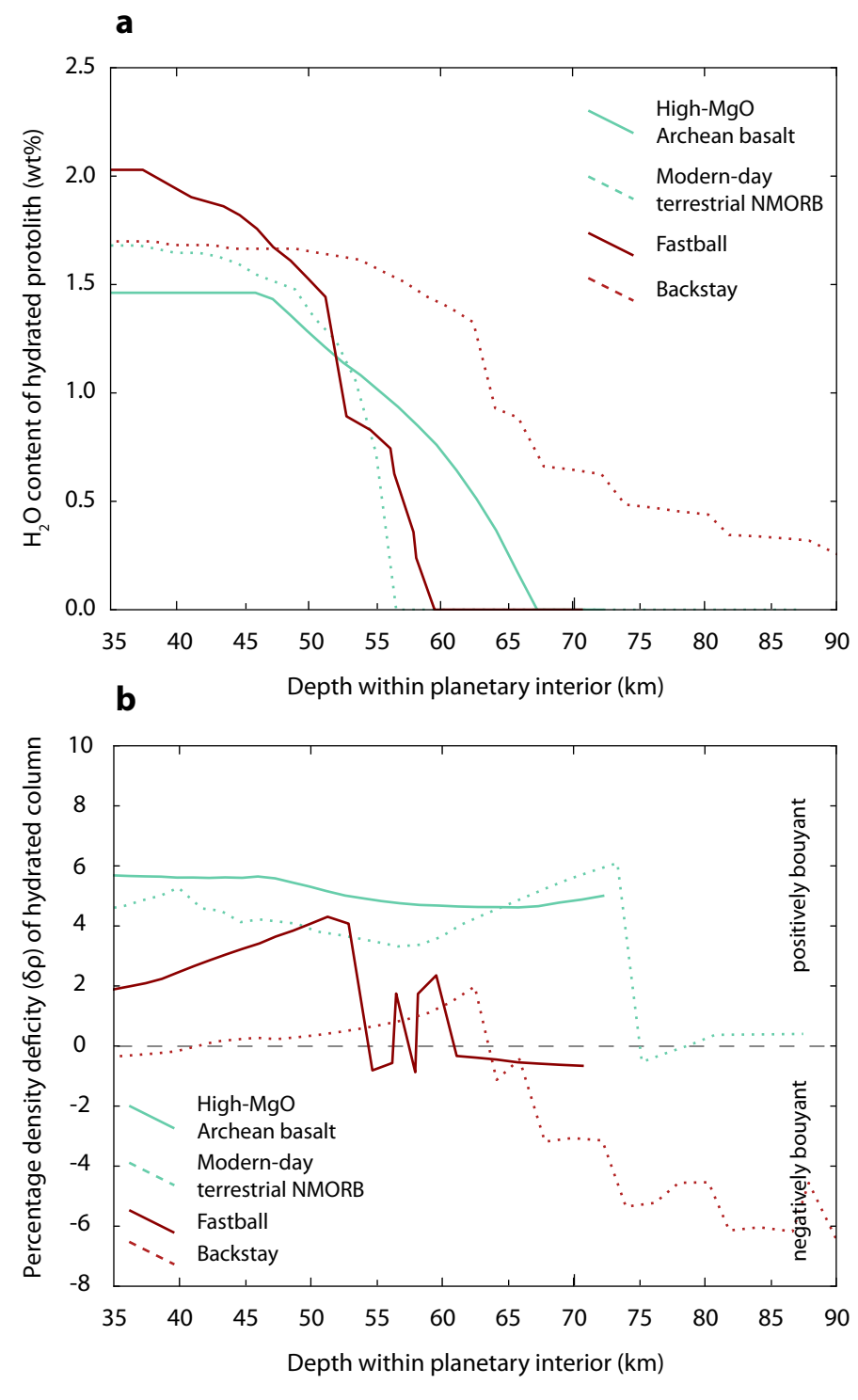
a
2.5
2.0
1.5
1.0
0.5
0.0
H2O content of hydrated protolith (wt%)
High-MgO
Archean basalt
Modern-day
terrestrial NMORB
Fastball
Backstay
35
40
45
50
55
60
65
70
75
80
85
90
Depth within planetary interior (km)
b
10
8
6
4
2
0
-2
-4
-6
-8
Percentage density deficity (δρ) of hydrated column
positively bouyant
negatively bouyant
High-MgO
Archean basalt
Modern-day
terrestrial NMORB
Fastball
Backstay
35
40
45
50
55
60
65
70
75
80
85
90
Depth within planetary interior (km)

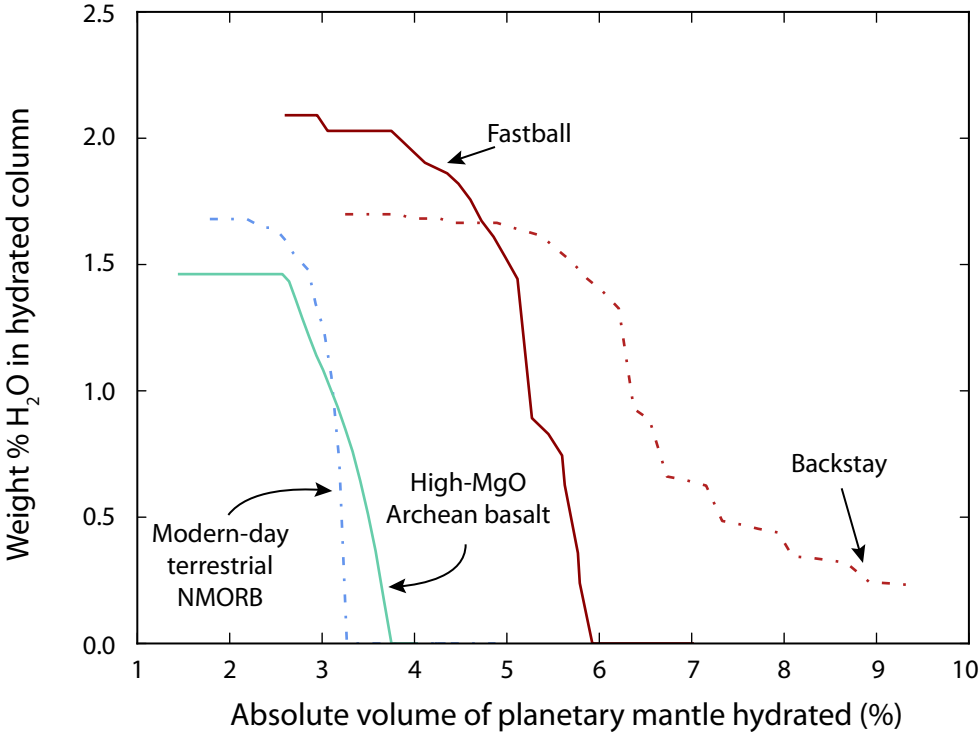
Weight % H_2O in hydrated column
2.5
2.0
1.5
1.0
0.5
0.0
1
2
3
4
5
6
7
8
9
10
Absolute volume of planetary mantle hydrated (%)
Fastball
Backstay
High-MgO
Archean basalt
Modern-day
terrestrial
NMORB

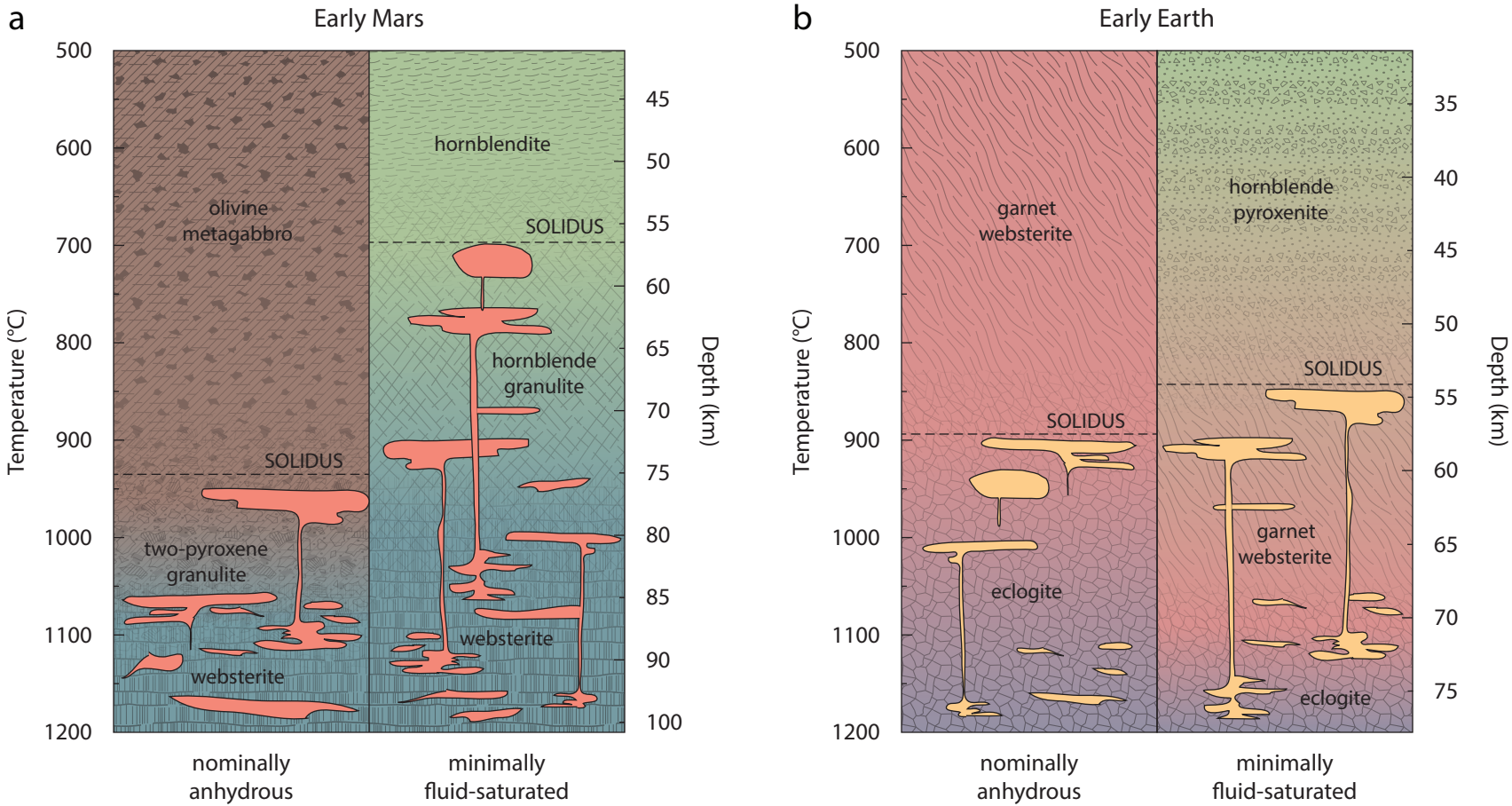
a
Early Mars
Temperature (°C)
Depth (km)
500
600
700
800
900
1000
1100
1200
45
50
55
60
65
70
75
80
85
90
100
olivine
metagabbro
SOLIDUS
two-pyroxene
granulite
websterite
hornblendite
SOLIDUS
hornblende
granulite
websterite
nominally
anhydrous
minimally
fluid-saturated
b
Early Earth
Temperature (°C)
Depth (km)
500
600
700
800
900
1000
1100
1200
35
40
45
50
55
60
65
70
75
garnet
websterite
SOLIDUS
eclogite
hornblende
pyroxenite
SOLIDUS
garnet
websterite
eclogite
nominally
anhydrous
minimally
fluid-saturated

METHODS

Petrological modelling procedures

All phase diagrams were constructed using THERMOCALC v. 3.45i[34] and the internally consistent thermodynamic data set ds62 (ref. [35]; updated 6/2/2012). Modelling was performed in the Na_2O–CaO–K_2O–FeO–MgO–Al_2O_3–SiO_2–H_2O–TiO_2–O_2 (NCKFMASHTO) compositional system using the following activity–composition relations for solid-solution phases: tonalitic melt, clinoamphibole, and augitic clinopyroxene[36], orthopyroxene, garnet, biotite, muscovite, chlorite, and ilmenite–hematite[37], plagioclase and K-feldspar[38], olivine and epidote[35], and spinel–magnetite[39]. Pure phases included albite, rutile, sphene, quartz, and H_2O. The initial bulk-rock compositions used for modelling of all protoliths were converted from wt. % oxides, as reported in each original study (Table 1, Extended Data), to mol. % oxides, with fluid contents adjusted on an individual basis, as described below. The software and data files used to generate the phase diagrams may be downloaded from http://www.metamorph.geo.uni-mainz.de/thermocalc

For modelling under water-present conditions (Table 2, Extended Data), bulk-rock fluid contents were individually fixed such that each lithology was minimally saturated at the intersection of the relevant geotherm/aerotherm and its solidus. Here, we define minimal saturation as the equilibrium phase assemblage containing 0.5 mol. % of free water (H_2O) at the point of first melting. Additional H_2O was present within the bulk-rock composition in each case as structurally bound water within hydrous minerals. For nominally anhydrous conditions, the absolute amount of H_2O within each bulk-rock composition was fixed at a total of 0.5 mol. % (prior to melt loss), with these bulk compositions shown in (Table 3, Extended Data). Invariably, free H_2O was absent from calculated assemblages, with all bulk-rock H_2O at the solidus being structurally bound within hydrous phases. For internal consistency and ease of comparison, calculations for all rock types used a molar bulk-rock $X\mathrm{Fe}^{3+}$ [= $Fe_2O_3/(Fe_2O_3+FeO)$] value of 0.1 (cf. refs. [40,41]). Uncertainty on the absolute positions of assemblage field boundaries in *P–T* space generally do not exceed ±1 kbar and ±50 °C for low variance equilibria at the 2σ level[42,43]. Such variation is largely a function of propagated uncertainty on end-member thermodynamic properties within the internally consistent dataset. However, as all phase diagrams were calculated using the same dataset and *a–x* relations, similar absolute errors associated with dataset end-members cancel, and calculated phase equilibria are expected to be relatively accurate to within ±0.2 kbar and ±10–15 °C[42,43].

The petrological effects of open-system melting and melt loss were modelled using manipulation of the read-bulk-info (RBI) matrix[44]. We assumed that melt loss was a cyclical process, with drainage events occurring each time a rock's melt proportion reaches a rheologically critical threshold. The melt-extraction threshold for intermediate and felsic magmas is around 20–30%[45,46], and we used the upper limit of this range (30%) as our transition point. Ten-percent of this melt was assumed to remain in the source rock following each drainage event, given that a minimum proportion of ~8% melt must be present in a rock in order to overcome the liquid percolation threshold[45]. From a computational standpoint, this was implemented by reducing the calculated modal proportion of the melt phase in the RBI matrix from 0.3 to 0.1 at each relevant *P–T* point along the relevant geotherm/aerotherm.

Petrological modelling: theory and application

The petrological modelling employed herein relies upon a thermodynamic-equilibrium model of metamorphism, in which it is assumed that equilibrium on a local scale is maintained among mineral, fluid, and melt phases during the evolution of the rock[47-50]. A model is used to represent the thermodynamics of each phase, comprising properties for its end-members combined with activity–composition (*a–x*) relations to describe their mixing in solid solution[51]. This allows calculation of the equilibrium compositions and proportions of phases (mineral, melt, and aqueous fluid) in the stable assemblage, at given pressure, temperature and bulk composition[52]. Equilibrium conditions in such a system require the equality of chemical potentials of each component in all phases, and must conform to the constraints of mass balance. Such calculations are frequently performed in metamorphic geology, with the help of appropriate software[34,52], to construct pseudosections: phase diagrams that map out the thermodynamically stable assemblages that would form in a particular bulk-rock composition across *P–T* space[50,53]. This calculation procedure and the *a–x* relations utilised are mature, and have been demonstrably effective in both forward (predictive) and inverse (descriptive) petrological modelling studies (cf. refs. [53-55] for representative examples). All phase abbreviations are after [56], alongside "L" or "Melt" for silicate melt.

Calculated bulk-rock density profiles

Calculated bulk-rock densities considered all phases in the equilibrium assemblage (solids, aqueous fluids, and melt) at each *P–T* point. Metamorphism of terrestrial NMORB in a hydrous system produces a relatively low density metamorphic product, owing to the abundance of H_2O leading to the formation of amphibole and biotite (Extended Data - Fig. 5). In contrast, relatively dense garnet and pyroxene form in the nominally anhydrous case (Extended Data - Fig. 6). We considered an open-system scenario in this work, whereby melt generated during metamorphism can reach a critical escape threshold and leave the local environment, which is a realistic approximation of a natural system. Differential degrees of melt-loss lead to a density inversion between terrestrial and Martian metabasalts at upper amphibolite-/granulite-facies conditions. As shown by our calculations, partial melting begins earlier (i.e. at lower temperature) in a hydrated NMORB than in a nominally anhydrous equivalent, owing to the abundance of amphibole in the former. In addition, melt generation is more voluminous, and quartz and feldspar are preferentially consumed as part of the melt-producing reactions. The density inversion for hydrous versus nominally anhydrous NMORB occurs at the point of first melt extraction, when the former becomes melt-depleted, and the residual phase assemblage is entirely anhydrous (Grt+Aug). As bulk-rock density was calculated for the entire petrological system (i.e. solid plus melt, prior to extraction), melt loss from the initially hydrated protolith causes the remaining solid residue to become denser than the initially nominally anhydrous equivalent, which has not yet accumulated sufficient melt to cause a drainage event. Density differences between both studied Martian basalts are also a result of bulk-rock composition and melt fertility, with the relatively high alkali content of the Fastball protolith producing low-density feldspars in anhydrous conditions, but relatively dense amphibole in a water-rich environment.

374 **Thermal modelling procedures**

375 The thermal model was constructed analytically as a solution to the one dimensional heat flow
376 problem in a plate[61], including an additional source term to account for radiogenic heat
377 production[62,63]

$$\frac{\partial T(x,t)}{\partial t} = \kappa \frac{\partial^2 T(x,t)}{\partial x^2} + A_0 \exp\left(-\frac{t-t_0}{\tau_r}\right)$$

378

379 where κ is the thermal diffusivity, t_0 is today, and A_0 is the present-day radiogenic heat
380 production rate with time constant τ_r[63]. We apply boundary conditions

$$T(x=0,t) = 0$$

$$T(x=L,t) = T_p \exp\left(-\frac{t-t_0}{\tau_s}\right)$$

381

382 where T_p is the mantle potential temperature, τ_s is the secular cooling time constant, and L is the
383 lithospheric thickness. Initial conditions at the time of lithospheric generation take into account
384 the secular cooling

$$T(x,t=0) = T_p \exp\left(-\frac{t-t_0}{\tau_s}\right)$$

385

386 with the same parameters as the boundary conditions above. The solution may be expressed as a
387 Fourier Series:

$$T(x,t) = T_p e^{-\frac{t-t_0}{\tau_s}}\left(\frac{x}{L}\right) + 2\sum_{n=1}^{\infty}\sin\left(\frac{\pi n x}{L}\right)\left[\frac{A_0\left((-1)^n-1\right)\tau_r\left(e^{-\frac{t-t_0}{\tau_r}} - e^{-n^2\pi^2\kappa t}\right)}{\left(\pi n - \pi^3\kappa n^3\tau_r\right)}\right.$$

$$\left. + \frac{T_p e^{-n^2\pi^2\kappa t}}{\pi n} + \frac{T_p\kappa(-1)^n\left(e^{-\frac{t-t_0}{\tau_s}} - e^{-n^2\pi^2\kappa t}\right)}{\pi n - \pi^3\kappa n^3\tau_s}\right] \quad (1)$$

388

389 which we evaluate the first 200 terms to produce each geotherm and aerotherm.
390
391 To explore the uncertainty on the radiogenic heat production and secular cooling rates, we
392 sampled 3240 geotherms and 3780 aerotherms, with a range of cooling rates on Earth of 20Ga <
393 τ_s < 45Ga and Mars of 10Ga < τ_s < 40Ga, and radiogenic heat production rates of 0.1μWm^{-3} < A_0
394 < 1.0μWm^{-3}. This resulted in a range of mantle potential temperatures for early Earth 1500°C <
395 T_p < 1600°C, late Earth 1300°C < T_p < 1400°C, early Mars 1600°C < T_p < 1700°C[64,65], and late
396 Mars 1350°C < T_p < 1450°C[66]. We then took the mean and 99% confidence interval of 150Ma
397 lithosphere for each family of thermal models, equivalent to a T_p of 1550/1650°C and
398 1350/1400°C for the primitive and evolved rocks of Earth/Mars respectively, as the input for the
399 petrological modelling and error estimates.
400
401 To assess the validity of a 1D model when used as an approximation for a spherical shell we
402 compared the steady state ($\tau_s \to \infty$, $t \to \infty$) solution of eqn (1) to the steady state spherical shell
403 solution,

$$T(r) = \frac{(R-L)(R-r)}{Lr}T_m \quad (2)$$

404

where R is the planetary radius, L the lithospheric thickness, and r the radial position. We found that the error obtained using a 1D approach compared to a spherical shell is 0.9% for the Earth and 1.77% for Mars, which is well within the uncertainty on the other parameters defined above.

Numerical simulations for the temperature structure were also calculated a posteriori from the results of the petrological modelling to account for depth dependent variations in the thermal diffusivity (κ) due to density variations in the bulk mineral assemblages. We found that the maximum deviation in the thermal structure due to compositional effects to be <1.5% for times after 10 Ma and thus could also be safely neglected, in agreement with other recent work[67].

Data Availability Statement: Authors can confirm that all relevant data are included in the paper and/ or its supplementary information files

REFERENCES.

34 Powell, R. & Holland, T. J. B. An internally consistent dataset with uncertainties and correlations: 3. Applications to geobarometry, worked examples and a computer program. *Journal of Metamorphic Geology* **6**, 173-204, doi:10.1111/j.1525-1314.1988.tb00415.x (1988).

35 Holland, T. J. B. & Powell, R. An improved and extended internally consistent thermodynamic dataset for phases of petrological interest, involving a new equation of state for solids. *Journal of Metamorphic Geology* **29**, 333-383, doi:10.1111/j.1525-1314.2010.00923.x (2011).

36 Green, E. C. R. *et al.* Activity-composition relations for the calculation of partial melting equilibria in metabasic rocks. *Journal of Metamorphic Geology* **34**, 845-869, doi:10.1111/jmg.12211 (2016).

37 White, R. W., Powell, R., Holland, T. J. B., Johnson, T. E. & Green, E. C. R. New mineral activity-composition relations for thermodynamic calculations in metapelitic systems. *Journal of Metamorphic Geology* **32**, 261-286, doi:10.1111/jmg.12071 (2014).

38 Holland, T. & Powell, R. Activity-composition relations for phases in petrological calculations: an asymmetric multicomponent formulation. *Contributions to Mineralogy and Petrology* **145**, 492-501, doi:10.1007/s00410-003-0464-z (2003).

39 White, R. W., Powell, R. & Clarke, G. L. The interpretation of reaction textures in Fe-rich metapelitic granulites of the Musgrave Block, central Australia: constraints from mineral equilibria calculations in the system K2O-FeO-MgO-Al2O3-SiO2-H2O-TiO2-Fe2O3. *Journal of Metamorphic Geology* **20**, 41-55, doi:10.1046/j.0263-4929.2001.00349.x (2002).

40 Berry, A. J., Danyushevsky, L. V., O'Neill, H. S. C., Newville, M. & Sutton, S. R. Oxidation state of iron in komatiitic melt inclusions indicates hot Archaean mantle. *Nature* **455**, 960-U942, doi:10.1038/nature07377 (2008).

41 Christie, D. M., Carmichael, I. S. E. & Langmuir, C. H. Oxidation-States of Midocean Ridge Basalt Glasses. *Earth and Planetary Science Letters* **79**, 397-411 (1986).

42 Powell, R. & Holland, T. J. B. On thermobarometry. *Journal of Metamorphic Geology* **26**, 155-179, doi:10.1111/j.1525-1314.2007.00756.x (2008).
43 Palin, R. M., Weller, O. M., Waters, D. J. & Dyck, B. Quantifying geological uncertainty in metamorphic phase equilibria modelling; a Monte Carlo assessment and implications for tectonic interpretations. *Geoscience Frontiers* **7**, 591-607, doi:10.1016/j.gsf.2015.08.005 (2016).
44 White, R. W. *Tutorial for using the readbulkinfo (rbi) script.*, <http://www.metamorph.geo.uni-mainz.de/thermocalc/tutorials/ - rbi> (2010).
45 Vigneresse, J. L., Barbey, P. & Cuney, M. Rheological transitions during partial melting and crystallization with application to felsic magma segregation and transfer. *Journal of Petrology* **37**, 1579-1600, doi:10.1093/petrology/37.6.1579 (1996).
46 Rosenberg, C. L. & Handy, M. R. Experimental deformation of partially melted granite revisited: implications for the continental crust. *Journal of Metamorphic Geology* **23**, 19-28, doi:10.1111/j.1525-1314.2005.00555.x (2005).
47 Khorzhinskii, D. S. *Physicochemical Basis of the Analysis of the Paragenesis of Minerals.* Consultants Bureau, (1959).
48 Thompson, J. B. Local equilibrium in metasomatic processes. *Researches in geochemistry* **1**, 427–457 (1959).
49 Guiraud, M., Powell, R. & Rebay, G. H2O in metamorphism and unexpected behaviour in the preservation of metamorphic mineral assemblages. *Journal of Metamorphic Geology* **19**, 445-454, doi:10.1046/j.0263-4929.2001.00320.x (2001).
50 Powell, R., Holland, T. & Worley, B. Calculating phase diagrams involving solid solutions via non-linear equations, with examples using THERMOCALC. *Journal of Metamorphic Geology* **16**, 577-588, doi:10.1111/j.1525-1314.1998.00157.x (1998).
51 Connolly, J. A. D. Multivariable phase diagrams – an algorithm based on generalized thermodynamics. *American Journal of Science* **290**, 666-718 (1990).
52 Connolly, J. A. D. Computation of phase equilibria by linear programming: A tool for geodynamic modeling and its application to subduction zone decarbonation. *Earth and Planetary Science Letters* **236**, 524-541, doi:10.1016/j.epsl.2005.04.033 (2005).
53 Palin, R. M. *et al.* High-grade metamorphism and partial melting of basic and intermediate rocks. *Journal of Metamorphic Geology* **34**, 871-892, doi:10.1111/jmg.12212 (2016).
54 Carson, C. J., Powell, R. & Clarke, G. L. Calculated mineral equilibria for eclogites in CaO-Na2O-FeO-MgO-Al2O3-SiO2-H2O: application to the Pouebo Terrane, Pam Peninsula, New Caledonia. *Journal of Metamorphic Geology* **17**, 9-24 (1999).
55 White, R. W., Powell, R., Holland, T. J. B. & Worley, B. A. The effect of TiO2 and Fe2O3 on metapelitic assemblages at greenschist and amphibolite facies conditions: mineral equilibria calculations in the system K2O-FeO-MgO-Al2O3-SiO2-H2O-TiO2-Fe2O3. *Journal of Metamorphic Geology* **18**, 497-511 (2000).
56 Kretz, R. Symbols of rock-forming minerals. *American Mineralogist* **68**, 277-279 (1983).
57 Kato, Y. & Nakamura, K. Origin and global tectonic significance of Early Archean cherts from the Marble Bar greenstone belt, Pilbara Craton, Western Australia. *Precambrian Research* **125**, 191-243, doi:10.1016/s0301-9268(03)00043-3 (2003).
58 Gale, A., Dalton, C. A., Langmuir, C. H., Su, Y. J. & Schilling, J. G. The mean composition of ocean ridge basalts. *Geochemistry Geophysics Geosystems* **14**, 489-518, doi:10.1029/2012gc004334 (2013).
59 Squyres, S. W. *et al.* Pyroclastic Activity at Home Plate in Gusev Crater, Mars. *Science* **316**, 738-742, doi:10.1126/science.1139045 (2007).
60 McSween, H. Y. *et al.* Alkaline volcanic rocks from the Columbia Hills, Gusev Crater, Mars. *Journal Of Geophysical Research-Planets* **111**, -, doi:Artn E09s91 Doi 10.1029/2006je002698 (2006).

61 Parsons, B. & Sclater, J. G. An analysis of the variation of ocean floor bathymetry and heat flow with age. *Journal of Geophysical Research* **82**, 803-827, doi:10.1029/JB082i005p00803 (1977).
62 Driscoll, P. & Bercovici, D. On the thermal and magnetic histories of Earth and Venus: Influences of melting, radioactivity, and conductivity. *Physics of the Earth and Planetary Interiors* **236**, 36-51, doi:10.1016/j.pepi.2014.08.004 (2014).
63 Michaut, C. & Jaupart, C. Secular cooling and thermal structure of continental lithosphere. *Earth and Planetary Science Letters* **257**, 83-96, doi:10.1016/j.epsl.2007.02.019 (2007).
64 Herzberg, C., Condie, K. & Korenaga, J. Thermal history of the Earth and its petrological expression. *Earth and Planetary Science Letters* **292**, 79-88, doi:10.1016/j.epsl.2010.01.022 (2010).
65 Lessel, J. & Putirka, K. New thermobarometers for martian igneous rocks, and some implications for secular cooling on Mars. *American Mineralogist* **100**, 2163-2171, doi:10.2138/am-2015-4732 (2015).
66 Filiberto, J. & Dasgupta, R. Constraints on the depth and thermal vigor of melting in the Martian mantle. *Journal of Geophysical Research: Planets* **120**, 109-122, doi:10.1002/2014je004745 (2015).
67 McKenzie, D., Jackson, J. & Priestley, K. Thermal structure of oceanic and continental lithosphere. *Earth and Planetary Science Letters* **233**, 337-349, doi:10.1016/j.epsl.2005.02.005 (2005).

[Extended Data – fig 1]

[Extended Data **– fig 1 legend]** Pressure–temperature (*P–T*) pseudosection calculated for the bulk-rock composition of Palaeoarchean high-Mg basalt sample 02MB256 from [57]. Some small fields are unlabelled for clarity. Bold dashed line labelled '*Early-Earth geotherm*' represents the *P–T* profile calculated via thermal modelling, and is enveloped by short-dashed lines representing upper and lower confidence intervals on these values.

[Extended Data – fig 2]

[Extended Data **– fig 2 legend]** Pressure–temperature (*P–T*) pseudosection calculated for the bulk-rock composition of NMORB from [58]. Some small fields are unlabelled for clarity. Bold dashed line labelled '*Modern-day terrestrial geotherm*' represents the *P–T* profile calculated via thermal modelling, and is enveloped by short-dashed lines representing upper and lower confidence intervals on these values.

[Extended Data – fig 3]

[Extended Data **– fig 3 legend]** Pressure–temperature (*P–T*) pseudosection calculated for the bulk-rock composition of Fastball from [59]. Some small fields are unlabelled for clarity. Bold dashed line labelled '*Early Martian aerotherm*' represents the *P–T* profile calculated via thermal modelling,

and is enveloped by short-dashed lines representing upper and lower confidence intervals on these values.

[Extended Data – fig 4]

[Extended Data **– fig 4 legend]** Pressure–temperature (*P–T*) pseudosection calculated for the bulk-rock composition of Backstay from [60]. Some small fields are unlabelled for clarity. Bold dashed line labelled '*Late-stage Martian aerotherm*' represents the *P–T* profile calculated via thermal modelling, and is enveloped by short-dashed lines representing upper and lower confidence intervals on these values.

[Extended Data – fig 5]

[Extended Data **– fig 5 legend]** Calculated mineral proportions, bulk-rock densities, and water contents during metamorphism of hydrated terrestrial and Martian basalts along their respective planetary geotherms and aerotherms.

Vertical dashed lines represent pressure–temperature (*P–T*) points at which melt extraction events occurred (see *Methods*).

[Extended Data – fig 6]

[Extended Data **– fig 6 legend]** Calculated mineral proportion and bulk-rock densities during metamorphism of nominally anhydrous terrestrial and Martian basalts along their respective planetary geotherms and aerotherms.

Vertical dashed lines represent pressure–temperature (*P–T*) points at which melt extraction events occurred (see *Methods*).

[Extended – Data table 1 – Title] Bulk compositions of mafic crustal components used in this work (weight % oxides).

[Legend]: - N.R. = not reported. [57]Kato and Nakamura (2003), sample 02MB256; [58]Gale et al. (2013); [59]Squyres *et al.* (2007); [60]McSween *et al*. (2006), Backstay "preferred composition".

[Extended – Data table 2 – Title] Bulk compositions used in phase equilibrium modelling (molar % oxides) under minimally fluid-saturated conditions.

[Legend]: - *N.B.* O contents were calculated assuming a bulk-rock $X\mathrm{Fe}^{3+} = \mathrm{Fe_2O_3}/(\mathrm{FeO}+\mathrm{Fe_2O_3}) = 0.1$, where $X\mathrm{Fe}^{3+} = (2 \times \mathrm{O})/\mathrm{FeO}^{tot}$. Stage numbers refer to the number of melt-extraction events, and the associated bulk compositions for numbers ≥1 represent increasingly melt-depleted residua (i.e. 0 = initial undepleted bulk composition; 1 = residual bulk composition following one melt-loss event, 2 = residual bulk composition following two melt-loss events etc.)

[Extended Data – Data table 3 – Title] Bulk compositions used in phase equilibrium modelling (molar % oxides) under nominally dry conditions.

[Legend]: *N.B.* O contents were calculated assuming a bulk-rock $X\mathrm{Fe}^{3+} = \mathrm{Fe_2O_3}/(\mathrm{FeO}+\mathrm{Fe_2O_3}) = 0.1$, where $X\mathrm{Fe}^{3+} = (2 \times \mathrm{O})/\mathrm{FeO}^{tot}$. Stage number nomenclature is the same as for Table S2.

595
596